The Astrophysical Journal, 970:66 (12pp), 2024 July 20 https://doi.org/10.3847/1538-4357/ad4d97

Unveiling the True Nature of Plasma Dynamics from the Reference Frame of a Superpenumbral Fibril

W. Bate[1], D. B. Jess[1,2], S. D. T. Grant[1], A. Hillier[3], S. J. Skirvin[4], T. Van Doorsselaere[4], S. Jafarzadeh[5,6], T. Wiegelmann[5], T. Duckenfield[1], C. Beck[7], T. Moore[1], M. Stangalini[8], P. H. Keys[1], and D. J. Christian[2]
[1] Astrophysics Research Centre, School of Mathematics and Physics, Queen's University Belfast, Belfast, BT7 1NN, UK; wbate02@qub.ac.uk
[2] Department of Physics and Astronomy, California State University Northridge, 18111 Nordhoff Street, Northridge, CA 91330, USA
[3] Department of Mathematics and Statistics, University of Exeter, Exeter, EX4 4QF, UK
[4] Centre for mathematical Plasma Astrophysics, Mathematics Department, KU Leuven, Celestijnenlaan 200B bus 2400, B-3001 Leuven, Belgium
[5] Max Planck Institute for Solar System Research, Justus-von-Liebig-Weg 3, 37077 Göttingen, Germany
[6] Niels Bohr International Academy, Niels Bohr Institute, Blegdamsvej 17, DK-2100 Copenhagen, Denmark
[7] National Solar Observatory, 3665 Discovery Drive, Boulder, CO 80303, USA
[8] ASI, Italian Space Agency, Via del Politecnico snc, 00133, Rome, Italy
Received 2024 March 1; revised 2024 April 29; accepted 2024 May 17; published 2024 July 17

Abstract

The magnetic geometry of the solar atmosphere, combined with projection effects, makes it difficult to accurately map the propagation of ubiquitous waves in fibrillar structures. These waves are of interest due to their ability to carry energy into the chromosphere and deposit it through damping and dissipation mechanisms. To this end, the Interferometric Bidimensional Spectrometer at the Dunn Solar Telescope was employed to capture high-resolution Hα spectral scans of a sunspot, with the transverse oscillations of a prominent superpenumbral fibril examined in depth. The oscillations are reprojected from the helioprojective Cartesian frame to a new frame of reference oriented along the average fibril axis through nonlinear force-free field extrapolations. The fibril was found to be carrying an elliptically polarized, propagating kink oscillation with a period of 430 s and a phase velocity of $69 \pm 4\,\mathrm{km\,s^{-1}}$. The oscillation is damped as it propagates away from the sunspot with a damping length of approximately 9.2 Mm, resulting in the energy flux decreasing at a rate on the order of $460\,\mathrm{W\,m^{-2}/Mm}$. The H$\alpha$ line width is examined and found to increase with distance from the sunspot, a potential sign of a temperature increase. Different linear and nonlinear mechanisms are investigated for the damping of the wave energy flux, but a first-order approximation of their combined effects is insufficient to recreate the observed damping length by a factor of at least 3. It is anticipated that the reprojection methodology demonstrated in this study will aid with future studies of transverse waves within fibrillar structures.

Unified Astronomy Thesaurus concepts: Solar fibrils (532); Solar oscillations (1515); Solar chromosphere (1479); Solar atmosphere (1477)

1. Introduction

Solar fibrils are thin, elongated structures observed in the chromosphere of the Sun, appearing as dark, thread-like features that trace the magnetic field lines above the solar surface (Jafarzadeh et al. 2017). Though prominent in regions of strong magnetic activity, such as sunspots or active regions (ARs), they are in fact ubiquitous across the solar disk. They are believed to be the manifestation of magnetic-field-aligned plasma density enhancements and are closely related to other solar features such as spicules. These similar features are often grouped under the umbrella term "fibrillar structures" (see, e.g., the recent review by Jess et al. 2023).

The exact physical processes that give rise to solar fibrils are still a subject of ongoing investigation (Tsiropoula et al. 2012). It is thought that they form due to the interaction of the plasma with the magnetic field lines, trapping denser plasma into field-aligned structures, giving the appearance of elongated structures (Leenaarts et al. 2015). What is clear is they are most abundant in the thin and diffuse chromosphere (Morton et al. 2012; Liu et al. 2014; Jess et al. 2015). In this dynamic region, fibrils have the potential to facilitate the transfer of energy between the photosphere and corona (Morton et al. 2014). Thus, they are a vital component to studies of energy transfer and deposition in the solar atmosphere since they act as visual tracers for wave phenomena.

Transverse magnetohydrodynamic (MHD) kink waves have been the subject of study in small-scale structures within sunspots. Pietarila et al. (2011) detected kink waves in dynamic fibrils near a sunspot, with a period of 135 s, using Ca II 854.2 nm observations from the Swedish Solar Telescope (SST). More recently, Morton et al. (2021a) employed high-resolution observations in the same spectral line from SST/CRISP to demonstrate the presence of transverse waves in sunspot superpenumbral fibrils, located in the solar chromosphere. They interpreted these oscillations as MHD kink modes, with average periods and propagation speeds of approximately 754 s and $25\,\mathrm{km\,s^{-1}}$, respectively. The velocity amplitudes, with an average of $0.76 \pm 0.47\,\mathrm{km\,s^{-1}}$, were observed to increase by about 80% with increasing distance from the center of the sunspot. Morton et al. (2021a) speculated that this variation might be due to a decrease in density along the fibrils as the superpenumbral region extends to higher atmospheric heights while moving away from the umbra, until it reaches the highest point of the magnetic canopy and returns to the surface. Hence, considering the field geometry in the chromosphere becomes crucial when interpreting these

observations, particularly in intensity images where projection effects are not readily apparent. Morton et al. (2021a) also discussed several potential excitation mechanisms for the transverse oscillations, such as convection-driven motions, magnetic reconnection, and mode conversion, ultimately finding the mode conversion mechanism to be the most convincing. It is worth noting that oscillations in these small-scale structures within sunspots may differ from those observed in other chromospheric features due to factors such as the exceptionally strong magnetic fields of a few kilogauss present in sunspots (Livingston et al. 2006).

Jafarzadeh et al. (2017) examine transverse oscillations of bright Ca II H fibrils in the vicinity of a forming sunspot with a similar magnetic topology to that of a sunspot, with median periods and velocity amplitudes of 83 ± 29 s and 2.4 ± 0.8 km s^{-1}, respectively, for oscillations within 134 fibrils. Propagating waves were able to be characterized in 23 fibrils, with median propagation speeds of 9 ± 14 km s^{-1}. Propagation in a single direction within each fibril was the most common occurrence, although counterpropagating waves within a single fibril, as well as standing waves, were also observed.

Finding the energy flux of fibril oscillations is an important step in investigating their contribution to the heating of the chromosphere and corona. It is estimated that an energy flux of 10^3–10^4 W m^{-2} is required to heat the chromosphere (Withbroe & Noyes 1977), an order of magnitude more than coronal requirements. It should be emphasized that this energy must be transported into the chromosphere and also dissipated there, i.e., it is not sufficient for the energy to simply travel through. This suggests that accounting for chromospheric heating is a challenge of equal or greater magnitude than for coronal heating when investigating solar atmospheric heating mechanisms.

An important caveat when interpreting any transverse energy flux estimates is that they are only based on resolved oscillations. Waves with amplitudes too small to be spatially resolved or periods too short to be temporally resolved are not included in these estimations, leaving the possibility that a significant amount of wave energy may be unaccounted for (Verth & Jess 2016). Another aspect contributing to the underestimation of the total energy flux may be the presence of kink motions along the observer's line of sight, which will not manifest as visible transverse oscillations. Examples of this have been documented by Sharma et al. (2018) and Shetye et al. (2021), who measured helical motions of spicules through Doppler measurements (see also the modeling work by Zaqarashvili & Skhirtladze 2008). If these line-of-sight motions are not taken into account when calculating the energy flux, it may result in an underestimation of the true value (Shi et al. 2021). Further, superposition of multiple features along the line of sight can result in an underestimation of the wave energy calculated from Doppler velocity oscillations by 1–3 orders of magnitude (De Moortel & Pascoe 2012; Pant et al. 2019).

In previous work, Bate et al. (2022) examined transverse kink oscillations within off-limb Hα spicules using imaging observations, and found that the energy flux of the upwardly propagating transverse waves decreases with atmospheric height at a rate of -13200 ± 6500 W m^{-2}/Mm. As a result, this decrease in energy flux as the waves propagate upwards may provide significant thermal input into the local plasma.

The aim of the current study is to expand on previous work on the energy flux of transverse waves within fibrillar structures. We aim to examine the properties of transverse oscillations of superpenumbral fibrils within three-dimensional space as they travel along the structures, allowing for the probing of their energy-carrying capabilities and any damping that may occur. Further, we aim to take advantage of the properties of the Hα line in order to probe the plasma temperature and search for signs of MHD wave energy dissipation. To achieve this objective, we utilize ground-based instrumentation with high spatial, spectral, and temporal resolutions, providing data products that are ideally suited for this study.

2. Observations

Observations were taken on 2015 September 16 with the Interferometric Bidimensional Spectrometer (IBIS; Cavallini 2006) at the Dunn Solar Telescope (DST) of the decaying AR NOAA 12418. The data were utilized by Beck & Choudhary (2020) and Prasad et al. (2022), where they are discussed in detail, thus only a short description is presented here. The IBIS field of view was placed over the leading sunspot of the group, located at $[x, y] = [-520'', -340'']$ with respect to solar disk center. The IBIS field of view consists of a circular aperture with a diameter of 95″ and a spatial sampling of 0.″095 per pixel. IBIS acquired data from 14:42 to 15:16 UT, with Hα spectral scans of 27 nonequidistant wavelength points. The exposure time at each wavelength position was 40 ms, with a full-scan cadence of 11.2 s, resulting in 400 scans being taken, with the majority under good seeing. All IBIS scans were coaligned by correlating subsequent images of the continuum intensity with each other. These coalignment corrections were minimal in nature due to the use of advanced adaptive optics (Rimmele & Marino 2011) utilized at the DST. The left panel of Figure 1 shows the Hα line-core intensity captured at 14:51 UT.

A single vector magnetogram was acquired at 14:46:19 UT using the Helioseismic and Magnetic Imager (HMI; Schou et al. 2012) on board the Solar Dynamics Observatory (SDO; Pesnell et al. 2012). This magnetogram was obtained with a spatial scale of 0.″5 per pixel. The full disk magnetogram was cropped to only include AR NOAA 12418 using the associated Space-weather HMI Active Region Patch (SHARP; Bobra et al. 2014). This was used to create a magnetic field extrapolation, detailed in Section 3.3.

3. Data Analysis

In the following subsections, we detail extensively the methodology employed to accurately fit the Hα spectral line (Section 3.1), isolate the fibrillar feature of interest (Section 3.2), and crucially reproject the fibril dynamics into a common reference frame based around its central axis (Section 3.3). These steps are fundamentally important to ensure robust consistency with future studies of fibrillar activity in mind.

3.1. Line Fitting

In a solar context, the Hα absorption line is known to be broadened by a number of factors, including turbulence, nonthermal, and thermal effects. The line shape is also affected by the fine and hyperfine structure of the $3 \rightarrow 2$ electronic transition. In addition, the line is also sensitive to strong magnetic fields, with an effective Landé factor of 1.06

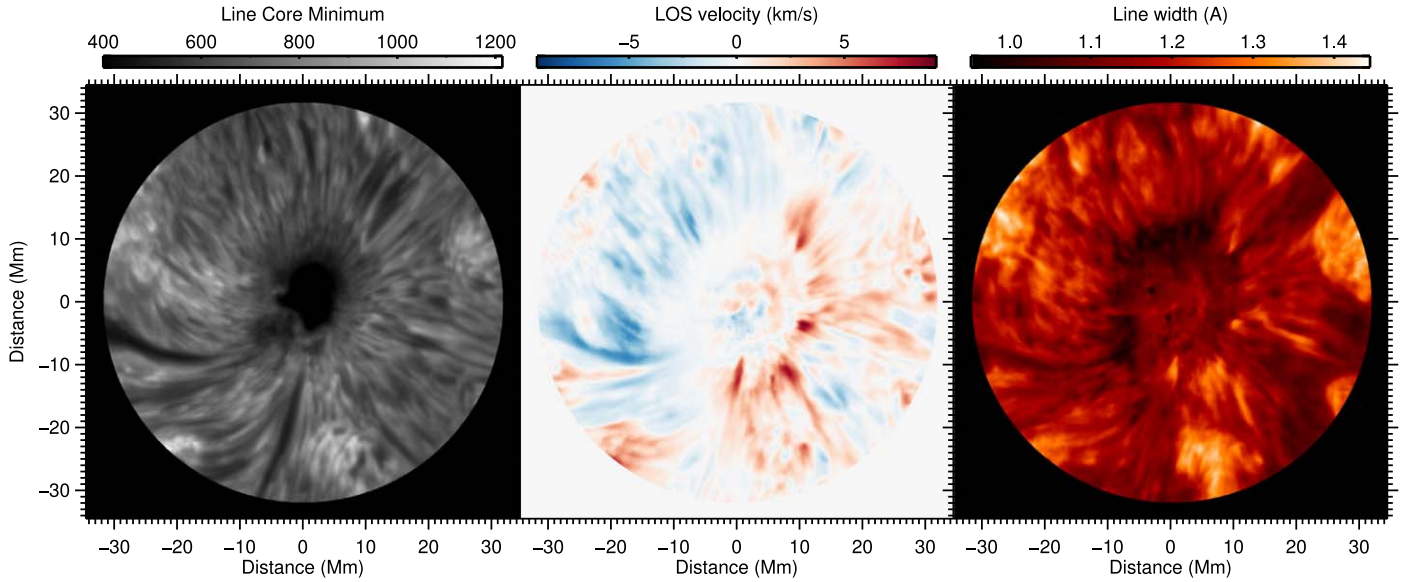

Figure 1. Data products derived from the IBIS field of view, acquired at 14:51 UT on 2015 September 16. The left panel shows the Hα line-core minimum found using the fit described by Equation (2). The middle panel displays the derived line-of-sight velocity from the parameter A_1 in Equation (2). The right panel shows the associated Hα line width in units of ångströms.

(Shenstone & Blair 1929; Landi Degl'Innocenti 1982; Lozitsky et al. 2018). This leads to the line shape not being fit well by typical line profiles such as the Gaussian, Lorentzian, or Voigt (Leenaarts et al. 2012). To illustrate this, a simple Gaussian fit of an example Hα profile is shown in blue in Figure 2, described by

$$f_G(\lambda) = -A_0 \exp\left(-\frac{(\lambda - A_1)^2}{2A_2^2}\right) + Q(\lambda), \quad (1)$$

where A_0 denotes the line depth, A_1 corresponds to the wavelength shift of the line-core position, A_2 is a parameter that is linearly related to the line width, and Q is a quadratic trend to aid with the fitting of the continuum.

It can be seen that the simple Gaussian profile demonstrated in Figure 2 systematically underestimates the line-core intensity and does not well represent the line width, with a consistent underestimation towards the line center and a consistent overestimation further out into the line wings.

As semiautomated analysis of the line shape, and especially the line width, was desired, many other potential functions to describe the Hα line profile were tested using a chi-squared goodness-of-fit test. The function that performed best is described as follows:

$$f_{SS}(\lambda) = -A_0 \operatorname{sech}^2\left(\left(\frac{(\lambda - A_1)^2}{2A_2^2}\right)^{A_3}\right) + Q(\lambda), \quad (2)$$

where A_3 is a parameter describing the steepness of the sides of the line profile between the core and continuum, and $A_{0,1,2}$ and Q have similar meanings to those in Equation (1). The function described by Equation (2) will henceforth be referred to as "super-sech" due to its similarity to a higher-order Gaussian (also known as a super-Gaussian). The mean-squared deviation (MSD) averaged over all line profiles in the data set was found to be 4170 for the super-sech profile, compared to an MSD of 12,990 for a simple Gaussian and 5250 for a higher-order

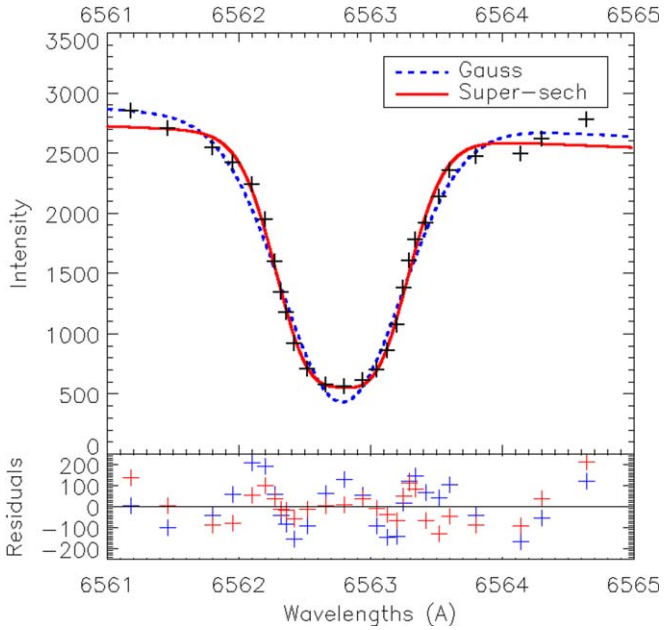

Figure 2. A demonstration of the line-fitting routines used on the Hα profile taken from a pixel within a fibril. In the upper panel, the pluses show the IBIS data, the dashed blue line shows a Gaussian profile fit described by Equation (1), and the solid blue line shows a super-sech profile fit described by Equation (2). The lower panel shows the residuals of these two fits with the same colors.

(or super-) Gaussian. This clearly demonstrates the suitability of Equation (2) over Equation (1) for fitting the Hα line profiles within this data set.

The prior estimates for the super-sech parameters ($A_{0,1,2}$) are taken from an initial fit using a simple Gaussian profile to reduce computational time. This is possible as the estimation of the central wavelength shift (A_1) is consistent between the Gaussian and super-sech fits, hence a Gaussian fit remains valid for any studies investigating line-of-sight velocities. This super-sech fitting routine will be made publicly available with

the release of WaLSAtools, anticipated for later this year (Jess et al. 2023).[9] Line-of-sight velocity ($v_{\rm LOS}$) and line width ($W_{\rm H\alpha}$) maps are shown in the central and right panels of Figure 1, respectively. Here, the line-of-sight velocity is calculated using the parameter A_1 in Equation (2).

The Hα line width is known to correlate with the plasma temperature (e.g., Leenaarts et al. 2012; Molnar et al. 2019; Pandit et al. 2023). Hence, the precision of the super-sech method of Hα line fitting allows for temperature inference through the derived methods described by Cauzzi et al. (2009). This method of line-width calculation was chosen for ease of comparison to the work of Molnar et al. (2019) and use of their derived relationship:

$$W_{\rm H\alpha} = 6.12 \times 10^{-5} \times T + 0.533, \quad (3)$$

where $W_{\rm H\alpha}$ is the width of the Hα line, and T is the brightness temperature observed in the Atacama Large Millimeter Array's (ALMA; Wootten & Thompson 2009) Band 3. This ALMA brightness temperature represents the electron temperature at the formation height of the 3 mm radiation (Loukitcheva et al. 2015; Wedemeyer et al. 2016). Only wavelengths within ± 1.0 Å of the nominal line-core wavelength were used in the calculation of the line width as this mirrors the methodology used in Molnar et al. (2019). Care must be taken when using this relationship, however, as the exact slope can vary depending on the solar structure imaged (Tarr et al. 2023).

3.2. Fibril Fitting

Individual fibrils were identified by examination of Hα line-core intensity images averaged over the length of the data set. This allows us to identify the fibrils that persist for a large proportion of the time, which is a useful condition for seeing many oscillation cycles, and further allows for the identification of their average axis position. An example fibril was chosen to best demonstrate the techniques used in the analysis of fibril oscillations. The calculated average fibril axis for this object was fit using cubic splines. Cross-cuts were then taken at multiple points along the fibril, with each cut perpendicular to the fibril axis in a similar mannner to the methodology utilized by Morton et al. (2021a). The example fibril, further discussed in Section 4, is shown in Figure 3 with the locations of the cross-cuts taken denoted by colored crosses.

This has allowed for the production of time–distance (TD) diagrams of line-core intensity (I_C), line-of-sight velocity ($v_{\rm LOS}$), and line width ($W_{\rm H\alpha}$) for each cut across the fibril, examples of which are shown in Figure 7, taken at the position of the green cross in Figure 3. The transverse deviations of the fibril from its average axis can be traced by fitting Gaussians to each time slice of the I_C TD diagrams in a method similar to that of Morton et al. (2013) and Weberg et al. (2018). These transverse motions are overplotted in each panel of Figure 7. The $v_{\rm LOS}$ and $W_{\rm H\alpha}$ values can then be read using the calculated transverse positions as a probe.

3.3. Reprojection to Fibril Axis Frame

Many previous works on the motion of fibrillar structures have utilized a helioprojective Cartesian (HPC) coordinate system (Thompson 2006). This is due to the ease of use when considering observations taken from only a single point and can be easily derived from the detector (CCD) coordinates. This approach, however, can "flatten" two main sources of projection effects, losing information about the fibrillar structure's motion in the process. These main projection effects are from (i) the angle between the solar normal and the observer's line-of-sight (the cosine of which is typically referred to as μ), and (ii) the angle between the axis of the fibrillar structure and the solar surface. In order to better discuss the three-dimensional motion of fibrils, a new coordinate system defined in terms of the fibril axis has been utilized, henceforth referred to as the fibril axis frame (FAF), and the process of its derivation and use is described below.

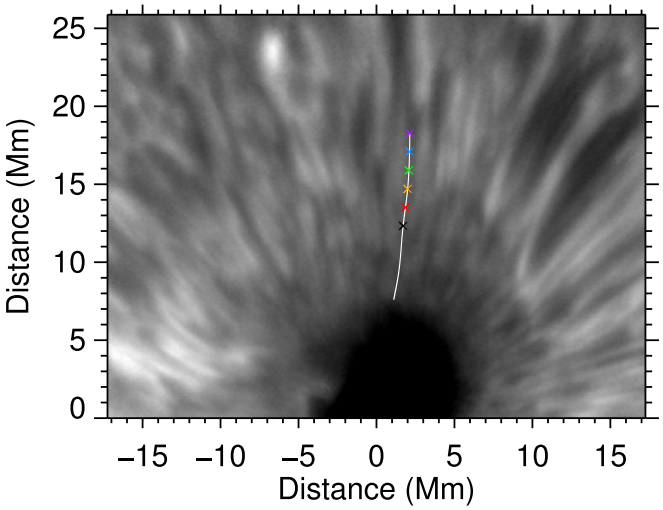

Figure 3. The example fibril analyzed in Section 4 is shown overplotted as a white line on a line-core Hα intensity image. The location of the cross-cuts that were taken are marked by colored crosses, with the colors corresponding to those in Figure 11.

A nonlinear force-free field (NLFFF; Wiegelmann et al. 2005; Wiegelmann 2008) extrapolation was performed in order to understand the angle of the fibril axis with respect to both the solar surface and the observer's line of sight (see Wiegelmann & Sakurai 2021, for a recent review of solar force-free fields). This is achievable as fibrils typically trace magnetic field lines (Leenaarts et al. 2012), and the penumbral region of sunspots exist in a low-plasma-β state (Gary 2001; Grant et al. 2018). This was achieved using data from the HMI (Scherrer et al. 2012) as well as SHARP (Bobra et al. 2014) for SHARP 5961, associated with AR NOAA 12418, shown in the top panel of Figure 4. The NLFFF extrapolation was performed utilizing the Lambert cylindrical equal-area (CEA) projection. The original vector magnetogram has been preprocessed in order to make it consistent with a force-free field in the corona (see Wiegelmann et al. 2006, for details). The NLFFF extrapolations have been carried out with the help of an optimization code. The force-free optimization principle has been described in Wheatland et al. (2000) and Wiegelmann (2004) and the NLFFF-code version specified for SDO/HMI (which we used here) in Wiegelmann et al. (2012).

The magnetic fields derived from the NLFFF model were reprojected into HPC coordinates in order to interpret the plane-of-sky and line-of-sight oscillations. This is a two-step process. First, the positions of each magnetic field vector were translated from CEA to HPC coordinates using SunPy's coordinates module (The SunPy Community et al. 2020),

[9] WaLSAtools website: https://walsa.team/codes.

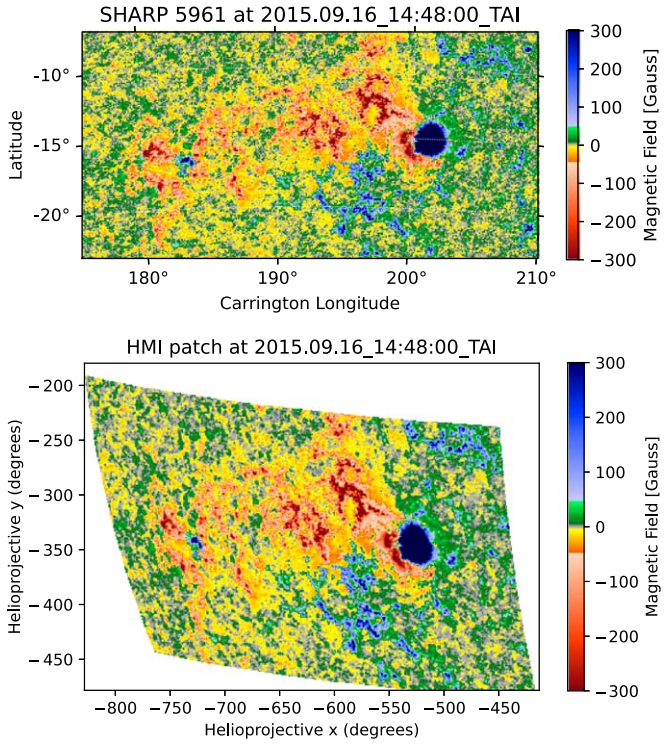

Figure 4. The top panel shows the HMI SHARP 5961, used for the NLFFF extrapolation. This is shown with the associated CEA coordinates. The lower panel shows this same patch used as a mask on HMI data and the associated helioprojective coordinates. The magnetic field in the upper panel is calculated with respect to an observer directly above the sunspot center; in the lower panel it is with respect to the line of sight of SDO. Both magnetic field values are cropped at ±300 G for clarity.

following a similar approach to that of Sun (2013). The resulting area covered in HPC coordinates is shown in the lower panel of Figure 4. Second, the magnetic field vectors were then transformed with the aid of a rotation matrix, $\mathcal{R}$. This was constructed for a transformation from the vector $\boldsymbol{u}$, which points from the solar center and through the center of the feature being examined in HPC coordinates, to the vector $\boldsymbol{v}$, which points from the solar center to the solar surface along the observer's line of sight. Hence, $\boldsymbol{u}$ and $\boldsymbol{v}$ are given by

$$\boldsymbol{u} = \begin{pmatrix} \vartheta_x & \vartheta_y & h \end{pmatrix}^T, \hat{\boldsymbol{u}} = \frac{\boldsymbol{u}}{|\boldsymbol{u}|}, \tag{4}$$

$$\boldsymbol{v} = \begin{pmatrix} 0 & 0 & \vartheta_{\rm limb} \end{pmatrix}^T, \hat{\boldsymbol{v}} = \frac{\boldsymbol{v}}{|\boldsymbol{v}|}, \tag{5}$$

where ϑ_x and ϑ_y are the x and y HPC coordinates of the feature under investigation, $\vartheta_{\rm limb}$ is the distance from solar center to the limb in HPC coordinates, and $h = \sqrt{\vartheta_{\rm limb}^2 - \sqrt{\vartheta_x^2 + \vartheta_y^2}}$. The directions of $\boldsymbol{u}$ and $\boldsymbol{v}$ are shown in Figure 5.

A mutually perpendicular vector, $\overrightarrow{\boldsymbol{s}}$, to both $\boldsymbol{u}$ and $\boldsymbol{v}$ was constructed as

$$\overrightarrow{\boldsymbol{s}} = \frac{\hat{\boldsymbol{u}} \times \hat{\boldsymbol{v}}}{|\hat{\boldsymbol{u}} \times \hat{\boldsymbol{v}}|}, \hat{\boldsymbol{s}} = \frac{\overrightarrow{\boldsymbol{s}}}{|\overrightarrow{\boldsymbol{s}}|} = \begin{pmatrix} s_0 & s_1 & s_2 \end{pmatrix}^T. \tag{6}$$

It should be noted that due to the construction of $\boldsymbol{u}$ and $\boldsymbol{v}$, s_2 is always equal to 0. This allows the construction of our rotation

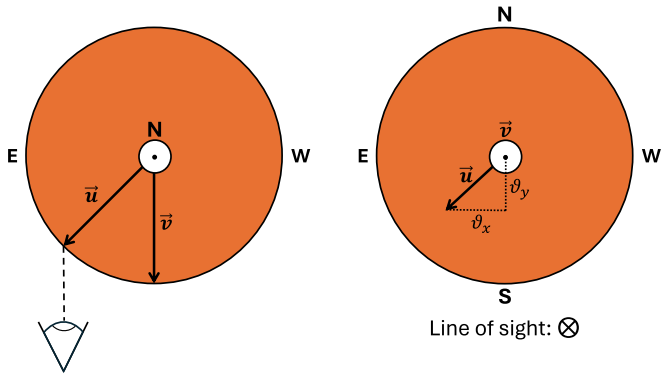

Figure 5. A schematic diagram to indicate the directions of the vectors $\boldsymbol{u}$ and $\boldsymbol{v}$, described by Equations (4) and (5), respectively. The left panel shows a top-down view of the Sun and the right panel shows the view from the direction of the Earth. Here, ⊙ represents a vector pointing out of the page, and ⊗ represents a vector pointing into the page.

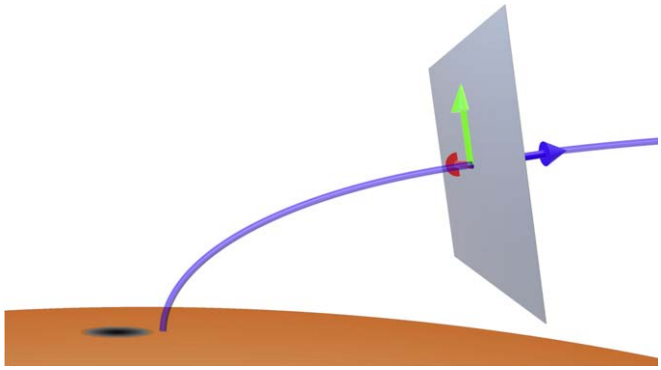

Figure 6. A cartoon of the FAF. The fibril axis is marked by the blue curved tube. The FAF x-, y-, and z-axes are shown by the red, green, and blue arrows, respectively. Note that the x-axis is parallel to the solar surface, and the z-axis is codirectional with the fibril axis and becomes more positive further from the sunspot. The FAF x, y plane is shown by the gray square.

matrix:

$$\mathcal{R} = \begin{pmatrix} \cos\theta + s_0^2(1-\cos\theta) & s_0 s_1(1-\cos\theta) & s_1 \sin\theta \\ s_1 s_0(1-\cos\theta) & \cos\theta + s_1^2(1-\cos\theta) & -s_0 \sin\theta \\ -s_1 \sin\theta & s_0 \sin\theta & \cos\theta \end{pmatrix}, \tag{7}$$

where θ is the angle between $\hat{\boldsymbol{u}}$ and $\hat{\boldsymbol{v}}$ (DeForest 2004; Riley et al. 2006).

Following this reprojection, the angle of the magnetic field (and hence the fibril) with respect to the line of sight of the observer was measured along a magnetic field line above each of the cross-cut locations, which are shown in Figure 3. This line was chosen by seeding magnetic field lines at each height above and below all cross-cut locations and selecting a field line that passes through all cross-cut locations and most closely matches the average fibril axis. This allows for the reprojection of all line-of-sight and plane-of-sky measurements into the FAF. As the name suggests, the FAF z-axis is oriented along the axis of the fibril, away from the sunspot (blue arrow in Figure 6). The FAF x-axis is perpendicular to the FAF z-axis and parallel to the solar surface (red arrow in Figure 6). The FAF y-axis is mutually perpendicular to both the FAF x-, z-axes (green arrow in Figure 6). The complete setup is visualized in Figure 6.

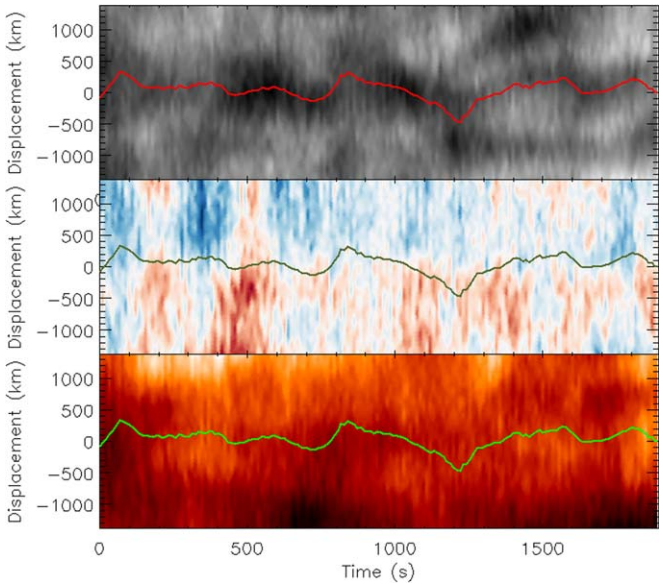

Figure 7. Time–distance diagrams illustrating the data analysis of a fibril oscillation, with a displacement of 0 km corresponding to the average fibril axis. The top panel shows line-core intensity, with the overplotted red line representing the calculated central position of the fibril as it undergoes FAF x-transverse oscillations. This same line is overplotted on the middle and bottom panels. The middle panel shows FAF y-velocity, and the bottom shows the Hα line width.

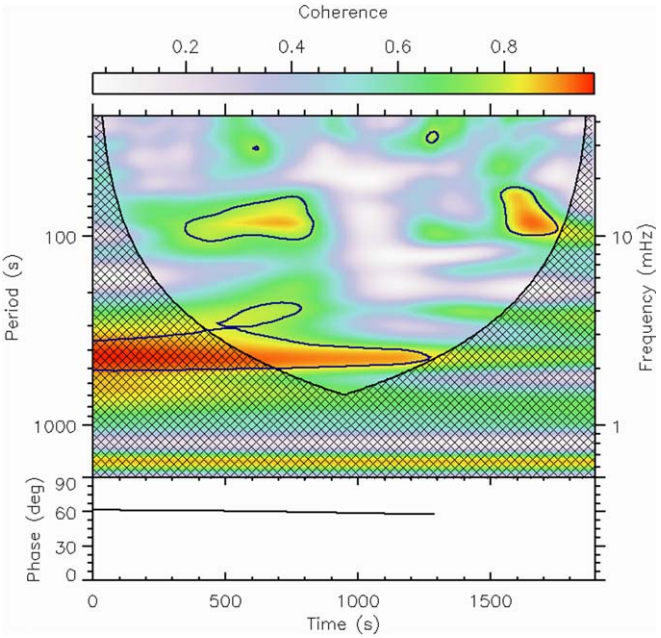

Figure 8. A cross-wavelet coherence spectrum between the FAF x-displacement and the FAF y-velocity measured at the cut location denoted by the green cross in Figure 3. The cone of influence is shown by the hashed region; the contour is at a 0.8 coherence level. The lower panel shows the phase angle measured at the dominant frequency (∼430 s) as a function of time.

4. Results

In the following subsections, the data-analysis techniques detailed in Section 3 are demonstrated through thorough analysis of a single fibril, shown by the white line in Figure 3. We detail the three-dimensional kink-like motion of the fibril in the FAF (Section 4.1), examine the trends of the Hα line width both as a function of distance and of time (Section 4.2), and use these observed oscillatory properties to estimate the energy flux carried by the fibril's oscillations (Section 4.3).

4.1. Kink Oscillations

Transverse oscillations were found to be near ubiquitous within the superpenumbral fibrils identified. An example fibril is shown in Figure 3 with the locations of the cross-cuts taken denoted by colored crosses and the fibril axis denoted by the white line. The magnetic field angles with respect to the solar surface at the heights and distances from the center of the sunspot considered within this study were found to be within the range 10°–40°, in agreement with Jess et al. (2013) and Morton et al. (2021a). The TD diagrams shown in Figure 7 were taken at the green cross shown in Figure 3. The magnetic field angle of this fibril at the green cross was found to be 22° with respect to the solar surface and −4° with respect to the plane of sky. As a result, all line-of-sight velocity measurements were adjusted by an appropriate factor, recasting $v_{\rm LOS}$ to a new v_y in the FAF, as detailed in Section 3.3.

Wavelet analysis (Torrence & Compo 1998) of the transverse oscillations at each of the cross-cut locations shows the same dominant period of ∼430 s. This is consistent with the median and modal periods, of 570 s and 330 s, respectively, found by Morton et al. (2021a) in superpenumbral fibrils. This is also consistent with the work of Jess et al. (2013), who found that longer-period (>180 s) waves were dominant in the sunspot penumbra and beyond, due to the effect of the magnetic field inclination on the acoustic cutoff frequency (Bel & Leroy 1977). Oscillations with a similar periodicity were also identified in the v_y oscillations. This then allowed for the use of cross-wavelet analysis to investigate the coherence of these oscillations as well as the phase lag between them. A cross-wavelet coherence spectrum is shown in Figure 8 comparing the transverse displacement (s_x) and v_y taken at the cross-cut denoted by the green cross in Figure 3. The 430 s oscillations are shown to be coherent and there is a phase lag of 60° between v_y and s_x, which is consistent at each cross-cut along the fibril. This phase lag also remains constant in time, as can be seen in the lower panel of Figure 8. Physically, this phase lag implies an elliptically polarized kink wave, with its semimajor and semiminor axes neither parallel or perpendicular to our FAF x-, y-axes (Lissajous 1857). Through further analysis, the velocity amplitude of the transverse displacement oscillations was found to be $v_{{\rm amp},x} = 1.6$ km s^{-1}, while the amplitude of the v_y oscillations was found to be $v_{{\rm amp},y} = 0.3$ km s^{-1}. This larger amplitude in the transverse direction is likely due to the suppression of FAF y-oscillations by the density stratification of the solar atmosphere. If the FAF x- and FAF y-oscillations were treated as two separate kink oscillations, then there would be approximately 30 times more energy flux carried by the FAF x-oscillation due to the energy flux being proportional to the square of the velocity amplitude (Van Doorsselaere et al. 2014).

In order to better illustrate the polarization of the transverse oscillation, a hodogram (or phase portrait) is presented in Figure 9. This was constructed through integration of v_y in order to calculate the FAF y-displacement, s_y. A hodogram was then produced following a similar method to that used by Zhong et al. (2023). The histogram distributions are shown at the bottom and on the right of each hodogram. The left panel shows the unfiltered data and the histograms shown are fitted with Gaussian distributions. The right panel has the data

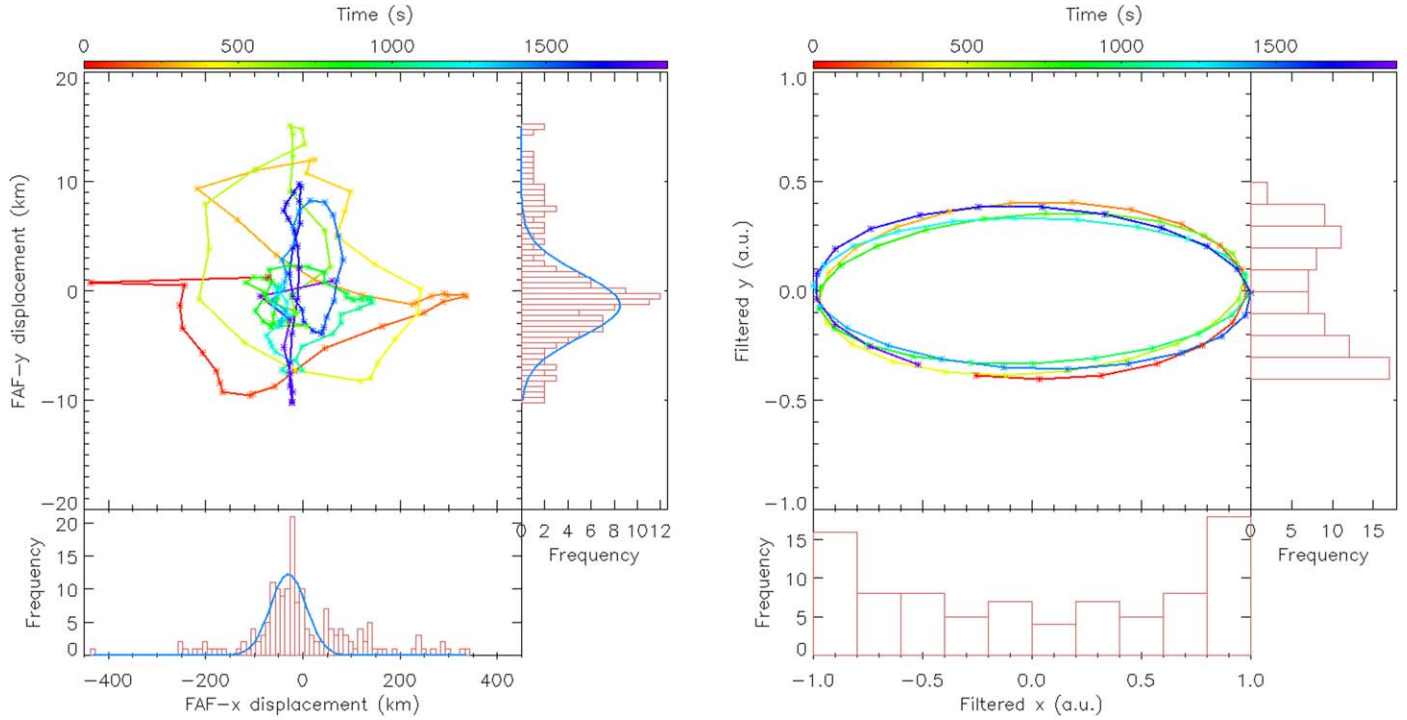

Figure 9. Hodograms representing the path that the fibril oscillation takes in the FAF x- and y-directions from an end-on view, i.e., the path it would trace out on the gray x, y plane marked in Figure 6. The left panel shows the raw data and the right panel shows the Fourier-filtered data for the 430 s oscillations under consideration. Time is represented by the colors indicated by the color bar at the top. The histograms on the bottom and right of each panel show how long the fibril spends at each of the FAF x- and y-positions, respectively. These measurements were taken at the location of the orange cross-cut in Figure 3. It should be noted that the amplitude of the oscillations in the FAF y-direction shown in the left panel are over an order of magnitude smaller than those in the FAF x-direction.

Fourier filtered for the 430 s oscillation under investigation. The x-axis range in the left panel is $[-450, 450]$ km, while the y-axis range is $[-20, 20]$ km. The units shown in the right panel are arbitrary. The bimodal nature of the histograms helps to confirm the elliptical nature of the oscillation, rather than a oblique-linear polarization (Zhong et al. 2023).

The phase speed, $v_{\mathrm{ph},z}$, of the oscillations along the FAF z-direction was calculated using phase-lag analysis (e.g., Vaughan & Nowak 1997). Similar cross-wavelet procedures were employed when comparing the s_x oscillations at different cut locations along the fibril length. The cross-wavelet coherence spectrum between s_x measured at the orange and green cross-cuts is shown in Figure 10. The phase lag, ϕ, was found to be 12° and was constant with time, as can be seen in the lower panel of Figure 10. This, combined with the distance along the FAF z-axis between the cut locations being $d_z = 1200$ km and knowledge of the period, $\mathcal{T}$, allows for the calculation (e.g., Mein 1977; Grant et al. 2015) of the phase speed as

$$v_{\mathrm{ph},z} = \frac{360 d_z}{\mathcal{T}\phi}. \tag{8}$$

It was found that the oscillation was traveling along the fibril away from the sunspot center, and $v_{\mathrm{ph},z}$ was calculated for each pair of adjacent cross-cuts along the fibril using the same cross-wavelet analysis shown for the green and orange cross-cuts in Figure 10. The phase speed of the transverse oscillations of the fibril was found to be constant along the length of the fibril at $69 \pm 4\,\mathrm{km\,s^{-1}}$. This lack of evidence for a change in propagation speed as a function of distance is in keeping with the findings of both Mooroogen et al. (2017) and Morton et al. (2021a). This value for the phase speed is in good agreement

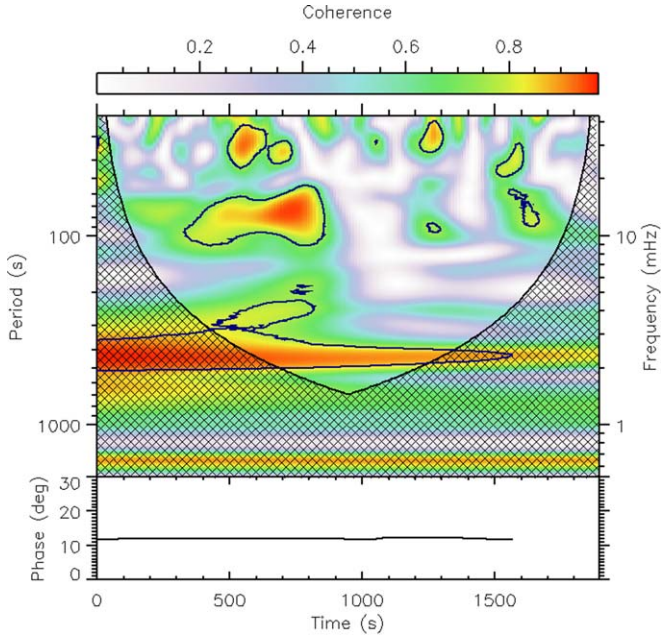

Figure 10. The same as Figure 8 but comparing the FAF x-oscillations measured at the locations of the orange and green crosses in Figure 3. The lower panel shows the phase angle measured at the dominant frequency (∼430 s) as a function of time.

with previous values for kink waves found in quiet-Sun and internetwork fibrillar structures found by Morton et al. (2012) and Kuridze et al. (2013). However, it is towards the higher end of the distribution of propagation speeds in superpenumbral fibrils calculated by Morton et al. (2021a), although this is

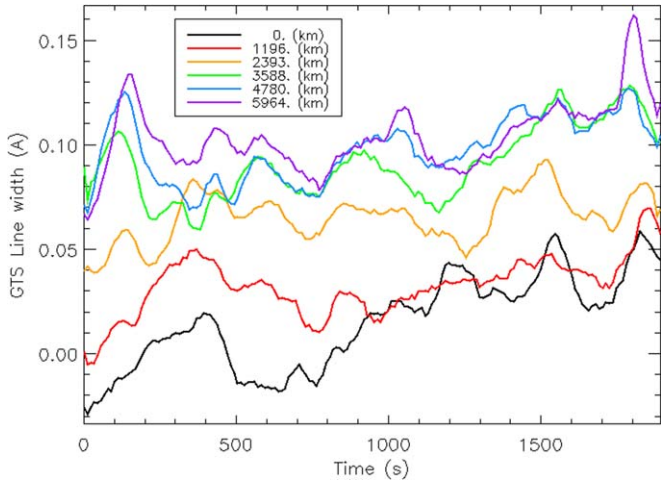

Figure 11. The GTS Hα line width calculated at different locations along the fibril. The colors correspond to those shown in Figure 3.

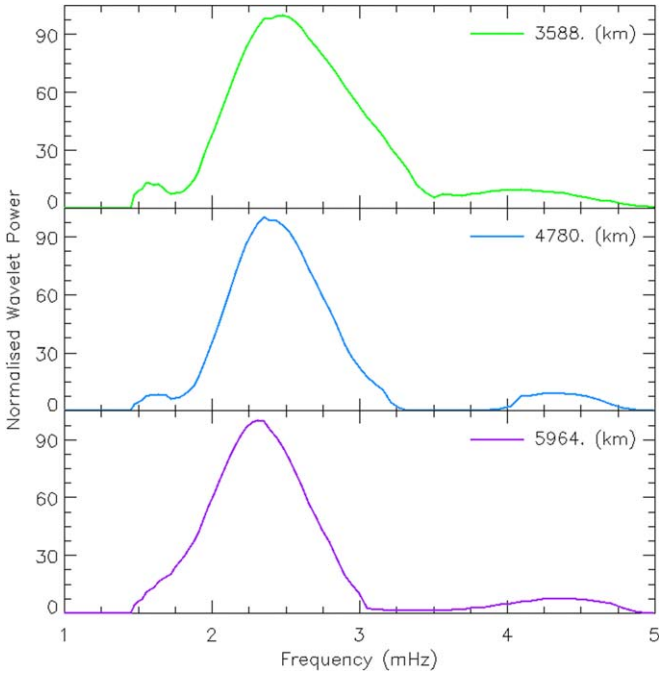

Figure 12. Wavelet power spectra calculated from the time series of Hα GTS line width shown in Figure 11. The colors correspond to the locations of the cross-cuts used for measurement shown in Figure 3. Each power spectrum shows a significant power at approximately 410 s.

likely due to their longer time cadence of 30 s. This phase velocity is much larger than that found in running penumbral waves of 5–20 km s^{-1} (Brisken & Zirin 1997; Jess et al. 2013).

4.2. Line-width Trend and Oscillation

The line width is seen to increase as we move away from the sunspot in all directions, as in the right panel of Figure 1. In order to account for this when considering the fibril alone, the average line width at each distance away from the sunspot was calculated over an arc of $\pi/2$ radians centered on the fibril axis. This average line width decreases at a rate of 0.009 Å/Mm with distance from the sunspot and shows no significant variation with time. This average value was then subtracted from the line width calculated at each cross-cut, resulting in a new quantity, henceforth referred to as global trend subtracted (GTS) line width. This subtraction of the background trend was performed in order to isolate local effects within the fibril from general trends in line width seen in the right panel of Figure 1 and ensures that the data plotted represent line-width variations intrinsically linked to the fibril itself. The GTS line width increases at a rate of 0.017 Å/Mm with distance along the fibril.

This new GTS line width at each of the cross-cut locations along the fibril is shown in Figure 11, with the color of each line corresponding to the locations denoted by the same color in Figure 3. The GTS line width can be seen to be increasing as a function of distance along the fibril. There is also a general trend of increasing GTS line width with time. The oscillations that can be seen in the GTS line width are believed to be due to an independent sausage-type oscillation coexisting within the fibril (Spruit 1982; Edwin & Roberts 1983; Jess et al. 2012; Morton et al. 2012; Sharma et al. 2018).

This periodicity was analyzed by computing power spectra of the GTS line width taken at the green, blue, and purple cross-cut locations in Figure 3 using a time integral of wavelet power, excluding regions influenced by cone of influence and only for those above the confidence level, resulting in a power-weighted frequency distribution (Torrence & Compo 1998). These power spectra are shown in Figure 12. A clear peak can be seen in the periodicity of each of these GTS line-width time series, located at a frequency consistent with a period of 410 s. This periodicity is extremely similar to that measured for the kink oscillation, 430 s. Further, phase-lag analysis (e.g., Vaughan & Nowak 1997) was undertaken and a phase lag of 8° was found between both sets of adjacent cross-cuts (green and blue, blue and purple). This allows the calculation of the phase velocity of this oscillation using Equation (8) as 130 km s^{-1}, propagating away from the sunspot. This is notably larger than the previously calculated phase speed of the kink oscillation, at 69 ± 4 km s^{-1}. This is not unexpected: Both the kink and sausage waves have phase speeds well above the typical chromospheric sound speed, identifying them as fast waves (Morton et al. 2012). In this regime, fast sausage waves have greater phase speeds than fast kink waves (Edwin & Roberts 1983), indicating the GTS line-width oscillations may be the signature of axisymmetric sausage modes.

If this was to be interpreted as a sausage mode detected concurrently with a kink mode within a fibril, then the similar periods of 410 s and 430 s, respectively, would be consistent with the findings of Morton et al. (2012), who found that their detected kink and sausage oscillations had periods of 232 ± 8 s and 197 ± 8 s, respectively. In order to conclusively associate the GTS line-width oscillations with a sausage oscillation, it was desired to observe a contemporaneous and coperiodic oscillation of the width of the magnetic cylinder, in this case our fibril (Edwin & Roberts 1983). However, no such oscillations were detected in our data set when following the methodology of Morton et al. (2012). This is likely due to any changes in fibril width being below the detection limit governed by the spatial resolution. Due to the uncertainty in the amplitude, we are unable to conclusively calculate the energy flux of the embedded sausage wave. Nevertheless, we present evidence of sausage-mode oscillations existing within the fibrillar structure, hence providing an interesting avenue of further investigation for future studies.

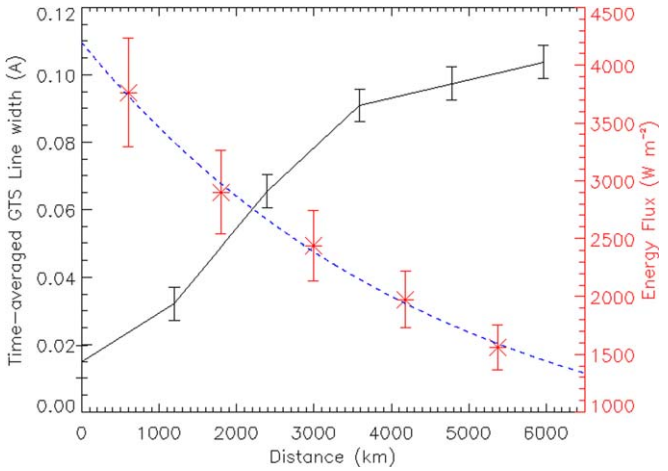

Figure 13. A comparison of time-averaged GTS line width at each distance, shown in black, with the energy flux carried by the kink wave calculated using Equation (9), shown in red. An exponential decay fit to the energy flux is shown by the blue dashed line.

4.3. Kink Energy Flux Estimation

By utilizing a model for the density of the fibril, following the variation with height above the solar surface according to Maltby et al. (1986), and by treating the displacement oscillations as a kink mode with velocity amplitude equal to the quadrature sum of the FAF x- and y-velocity amplitudes, the energy flux, F, of the oscillation can be calculated as

$$F \approx f\frac{1}{2}\rho_i v_{\rm amp}^2 v_{{\rm ph},z}, \tag{9}$$

where ρ_i is the density inside the fibril, and f is the filling factor that was taken as 5% to remain consistent with previous literature values (e.g., Van Doorsselaere et al. 2014; Bate et al. 2022; Magyar et al. 2022).

The time-averaged GTS line width and the energy flux are presented as a function of distance in Figure 13. The line width increases at an average rate of 0.017 Å/Mm. As noted in Section 3.1, care must be taken when using the relationship presented in Equation (3) as different gradients have been found for different Hα data sets (Tarr et al. 2023). However, assuming that Equation (3) holds for the purposes of temperature comparison, we arrive at a temperature increase rate of approximately 250 K/Mm. Although, as mentioned previously, nonthermal effects can contribute to line width, relevant simulations have found that temperature increase is the dominant source of line broadening when compared to small-scale turbulence (e.g., Antolin et al. 2017).

The energy flux is seen to decrease at an average rate of 460 W m^{-2}/Mm. This increase in GTS line width, coupled with a decrease in the energy flux carried by the kink waves, appears to be a signature of MHD wave damping in the form of plasma thermalization.

As is shown by the blue dashed line in Figure 13, the energy flux decay can be approximated by an exponential decay as a function of distance, with a scale height of 4.6 Mm. A linear damping mechanism would correspond to such an exponential decay, whereas a nonlinear damping mechanism would result in a different decay profile (Hillier et al. 2024). However, it is difficult to infer the true nature of the relationship with only five data points. Due to energy flux being proportional to the square of velocity amplitude in Equation (9), this energy scale height of 4.6 Mm implies a damping length of 9.2 Mm.

5. Theoretical Mechanisms for Wave Damping

Circularly polarized propagating kink waves have been observed before in chromospheric magnetic elements (Stangalini et al. 2017). These circularly/elliptically polarized kink modes should not be unexpected as, even if all kink modes are initially linearly polarized, circular polarization will evolve in magnetic structures with twisted magnetic fields or rotational flows (Ruderman & Terradas 2015). Further, expansion of the magnetic feature hosting linearly polarized kink modes can result in elliptical polarization arising (e.g., Russell et al. 2015). Another excitation mechanism for elliptically polarized kink waves is the combination of two or more kink pulses with different orientations and amplitudes superimposed within the same magnetic flux tube (Zaqarashvili & Skhirtladze 2008; Stangalini et al. 2017). Magyar et al. (2022) examine the dynamics of circularly polarized standing kink waves and their damping. They find that through the damping of these circularly polarized waves, elliptical polarization again develops.

There are many proposed mechanisms for the damping of kink (or Alfvénic) waves (see the recent review by Morton et al. 2023, and references therein). By treating fibrils as magnetic cylinders embedded within the solar chromosphere, this plasma inhomogeneity results in more effective damping than Alfvén waves would otherwise experience in a uniform medium. It should be noted that this damping does not necessarily imply the deposition of wave energy into the plasma as heating. Here, we explore the different theoretical mechanisms for wave damping and attempt to interpret how these would affect the kink oscillation of a fibril both independently and through their interplay.

5.1. Resonant Absorption

Within our magnetic cylinder approximation of an oscillating fibril, resonant absorption relies on the existence of a continuous variation of the Alfvén speed perpendicular to the magnetic field (as opposed to a discrete step function at the boundary of the cylinder). This will be assumed to be achieved by a variation of density, ρ, for further calculations in this subsection (Goossens et al. 2011). Resonant absorption as a wave-damping mechanism relies on the energy of a global MHD wave (in this case, a kink wave) being transferred into small-scale resonant Alfvén waves that then lead to dissipation. These small-scale waves may also result in line broadening (Griem 2005).

The oscillations analyzed in Section 4 lie firmly within the long-wavelength regime ($R/\lambda \ll 1$), where R is the radius of the fibril and λ is the wavelength of the kink wave (Terradas et al. 2010). This allows for the use of the Terradas–Goossens–Verth (TGV) relation, given by

$$L_D = v_{{\rm ph},z}\frac{2}{\pi}\frac{1}{m}\frac{R}{l}\frac{\rho_i+\rho_e}{\rho_i-\rho_e}\frac{1}{\nu}, \tag{10}$$

where R is the radius of the fibril, l is the width of the inhomogeneous surface layer, $\rho_{i,e}$ are the internal and external densities, respectively, and ν is the frequency of the oscillation (Verth et al. 2010; Tiwari et al. 2019).

As the exact density contrast, $\zeta = \rho_i/\rho_e$, is unknown, a range of values are considered. The factor $(\rho_i + \rho_e)/(\rho_i - \rho_e)$ varies between 2 and 1 for a density contrast range of $\zeta = [3, \infty)$. This allows for the consideration of all sensible density contrast values. The width of the boundary layer is also unknown, but a range of values $l/R = [1/3, 1/2]$ is considered (e.g., Magyar & Van Doorsselaere 2016; Morton et al. 2021b).

Using this relationship, assuming a pure kink mode ($m = 1$), a range of damping lengths between 38 and 113 Mm due to resonant absorption is calculated. The most effective damping (and thus the shortest damping length) corresponds to the case $\zeta \to \infty$ and $l/R = 1/2$. Through the recasting of this damping length as a damping time, valid for cases of weak damping (e.g., Morton et al. 2021b), the damping time due to resonant absorption can be calculated as $\tau_R = 550$–1650 s.

The calculated damping length due to resonant absorption far exceeds the observed damping length, even in the most extreme case, calculated from the relationship shown in Figure 13 as 9.2 Mm. It should be noted, however, that Equation (10) is formulated under the assumption of weak damping (Van Doorsselaere et al. 2004; Soler et al. 2013). This indicates that resonant absorption of pure kink modes is not responsible for the damping reported in this study. However, as can be seen from Equation (10), higher-order fluting modes ($m > 1$) damp due to resonant absorption over shorter length scales than pure kink modes. Pure fluting modes in a magnetic cylinder are surface-like, and in smooth boundary cases (such as our $l/R = [1/3, 1/2]$ assumption), these modes are likely not able to be supported (Soler 2017). However, numerical simulations along with analytic theory suggest that kink motions can couple with fluting modes nonlinearly, resulting in a fraction of the kink-mode energy being converted to fluting modes and the production of "mixed modes," so this route of wave damping via mode conversion cannot be discounted (Ruderman et al. 2010; Ruderman 2017; Terradas et al. 2018).

The damping due to ion–neutral collisions (Cowling's diffusion) has not been considered here, as it has been found through theoretical studies to be negligible when compared to the damping due to resonant absorption (Soler et al. 2011, 2012).

5.2. Uniturbulence

In a uniform medium, Alfvén wave turbulence is generally understood to arise from the nonlinear interaction of counter-propagating Alfvén waves (Iroshnikov 1964; Kraichnan 1965). This is typically understood through use of the Elsässer formalism. In an incompressible, homogeneous plasma, pure Alfvén waves are described by either one of the Elsässer variables, with z^- corresponding to propagation parallel to the magnetic field and z^+ to antiparallel propagation. A necessary condition for the formation of turbulence is that both $z^{\pm}$ are nonzero, hence the need for counterpropagating waves.

However, the solar atmosphere is not well described by an incompressible, homogeneous plasma, and so further refinements are required. Perpendicular inhomogeneities with respect to the magnetic field can also give rise to Alfvénic wave turbulence, such as in the case of a magnetic cylinder interpretation of a fibril. This is due to the inhomogeneity allowing for both $z^{\pm}$ to be nonzero for a kink wave propagating in a single direction. Unidirectionally propagating kink waves can be damped by so-called "uniturbulence" (Magyar et al. 2017, 2019), which is a nonlinear damping mechanism with an energy cascade damping time given by Van Doorsselaere et al. (2020, 2021a) as

$$\tau_U = 2\sqrt{5\pi}\frac{2R}{v_{\rm amp}}\frac{\rho_i + \rho_e}{\rho_i - \rho_e}. \tag{11}$$

The nonlinearity of this damping mechanism is made clear by the influence of the velocity amplitude, $v_{\rm amp}$, in Equation (11). This interpretation of τ_U as a damping time relies on the assumption of an exponential decay profile due to this nonlinear damping mechanism, something which cannot hold, but is an approximation made for comparison with linear damping mechanisms (Van Doorsselaere et al. 2021a).

By utilizing the same range of density contrasts, $\zeta = [3, \infty)$, as in the damping length calculation of Section 5.1, and our largest calculated velocity amplitude, $v_{\rm amp} = 1.9$ km s^{-1}, we are able to calculate a damping time range of $\tau_U = 1400$–2800 s. This is noticeably larger than the τ_R of 550–1650 s previously calculated. This is in good agreement with the study by Morton et al. (2021b), which found that τ_R/τ_U is typically less than 1 for propagating kink modes. It should also be noted that the strength of damping due to uniturbulence decreases for smaller velocity amplitudes, decreasing in its effectiveness by almost a factor of 2 for the smallest calculated velocity amplitude of $v_{\rm amp} = 1.2$ km s^{-1}.

5.3. Combination of Damping Mechanisms

If the contribution of two damping mechanisms is small and independent, it is possible to combine their effects following the methodology of Van Doorsselaere et al. (2021b) and Morton et al. (2021b). This assumption of independence may not be entirely justified due to the effects of resonant absorption on the development on turbulence, but will prove useful as a first-order approximation (Antolin & Van Doorsselaere 2019). It also assumes that the damping effects of both mechanisms result in exponential damping profiles, something which does not hold for nonlinear damping, but due to the relatively weak effect of the nonlinear damping this should not invalidate its results (Morton et al. 2021b). This approach combines the damping times due to resonant absorption (see Section 5.1) and the dominant nonlinear damping mechanism of uniturbulence (see Section 5.2) using the following to calculate the overall damping time, τ_T, as follows:[10]

$$\frac{1}{\tau_T} = \frac{1}{\tau_R} + \frac{1}{\tau_U}. \tag{12}$$

Following this approach, we arrive at $\tau_T = 400$–1050 s. Recasting this as a damping length gives a value of 27–71 Mm. Although this is shorter than the damping length derived from resonant absorption and uniturbulence individually, even in the most extreme case it is a factor of 3 longer than the damping length of 9.2 Mm derived from the relationship shown in Figure 13. This is likely due to the more complex interplay between different damping mechanisms, other damping mechanisms not considered, or different values of density contrast (ζ) and boundary layer thickness (l) being the case for the fibril considered.

[10] It should be noted that previous works (e.g., Van Doorsselaere et al. 2021b; Morton et al. 2021b) refer to this relationship as a "harmonic average," however this relationship is distinct from the more common definition of a harmonic mean by a factor of 2.

6. Conclusions

Here, we provide an in-depth case study of a transverse fibril oscillation and provide numerous techniques to help analyze its motion. There are a large number of previous studies of transverse waves within fibrillar structures. Through magnetic field modeling via a NLFFF extrapolation and consideration of the effect of the solar μ angle, the transverse oscillation characteristics have been reprojected into the FAF. This has allowed for the alleviation of projection effects that would be suffered when performing a standard helioprojective study. It is anticipated that this technique can further inform future works on the topic, helping to move away from a simple line-of-sight and plane-of-sky analysis. The in-depth discussion of this methodology should allow for its use in larger statistical studies of the oscillations of fibrillar structures, without the major concern of projection effects.

This has allowed an elliptically polarized kink wave of a superpenumbral fibril to be resolved and its propagation away from the sunspot center to be characterized, with a phase lag of 60° between the FAF x- and y-motions and a period of 430 s. This represents the first observation of an elliptically polarized kink wave within a chromospheric fibril using properly translated motions. These observed and calculated oscillation parameters have facilitated the calculation of the energy flux carried by this kink wave as it propagates in the FAF z-direction at a phase velocity of $v_{\mathrm{ph},z} = 69 \pm 4$ km s^{-1} and its associated damping length of $L_D = 9.2$ Mm. Further, through the use of a novel "super-sech" function for the fitting of the Hα line profile, an increase in the GTS line width has been tracked, showing an increase with distance along the fibril in the FAF z-direction. This is an indicator of wave damping occurring alongside plasma thermalization, although further work is necessary to ascertain whether the two processes are linked through energy dissipation.

Different mechanisms have been explored for the damping of the energy flux carried by the wave, with resonant absorption and uniturbulence considered as the dominant linear and nonlinear mechanisms, respectively. However, through a first-order approximation of their combined effect, we arrive at a shortest theoretical damping length of 27 Mm. This is 3 times longer than the observed damping length, even for the most extreme combination of parameters considered, demonstrating that further analysis of potential damping mechanisms and their interplay is warranted.

As mentioned previously, it is anticipated that the techniques and methodology here can be used to inform future studies of the ubiquitous transverse waves found within fibrillar structures. The Hα profile fitting and the FAF reprojection code will be made publicly available with the upcoming release of WaLSAtools (Jess et al. 2023).

Acknowledgments

W.B., D.B.J., and T.D. acknowledge support from the Leverhulme Trust via the Research Project grant No. RPG-2019-371. D.B.J. and S.D.T.G. wish to thank the UK Science and Technology Facilities Council (STFC) for the consolidated grant Nos. ST/T00021X/1 and ST/X000923/1. D.B.J. and S.D.T.G. also acknowledge funding from the UK Space Agency via the National Space Technology Programme (grant No. SSc-009). A.H. is supported by STFC Research grant No. ST/V000659/1. T.V.D. received financial support from the Flemish Government under the long-term structural Methusalem funding program, project SOUL: Stellar evolution in full glory, grant No. METH/24/012 at KU Leuven, the DynaSun project (number 101131534 of HORIZON-MSCA-2022-SE-01), and also a Senior Research Project (grant No. G088021N) of the FWO Vlaanderen. T.W. acknowledges DLR grant No. 50OC2301. The Dunn Solar Telescope at Sacramento Peak/NM was operated by the National Solar Observatory (NSO). NSO is operated by the Association of Universities for Research in Astronomy (AURA), Inc., under cooperative agreement with the National Science Foundation (NSF). Finally, we wish to acknowledge scientific discussions with the Waves in the Lower Solar Atmosphere (WaLSA; https://www.WaLSA.team) team, which has been supported by the Research Council of Norway (project no. 262622), The Royal Society (award no. Hooke18b/SCTM; Jess et al. 2021), and the International Space Science Institute (ISSI Team 502).

Facility: Dunn (IBIS; Cavallini 2006), HMI (HMI; Schou et al. 2012)

ORCID iDs

W. Bate https://orcid.org/0000-0001-9629-5250
D. B. Jess https://orcid.org/0000-0002-9155-8039
S. D. T. Grant https://orcid.org/0000-0001-5170-9747
A. Hillier https://orcid.org/0000-0002-0851-5362
S. J. Skirvin https://orcid.org/0000-0002-3814-4232
T. Van Doorsselaere https://orcid.org/0000-0001-9628-4113
S. Jafarzadeh https://orcid.org/0000-0002-7711-5397
T. Wiegelmann https://orcid.org/0000-0001-6238-0721
T. Duckenfield https://orcid.org/0000-0003-3306-4978
C. Beck https://orcid.org/0000-0001-7706-4158
T. Moore https://orcid.org/0000-0001-8385-3727
M. Stangalini https://orcid.org/0000-0002-5365-7546
P. H. Keys https://orcid.org/0000-0001-8556-470X
D. J. Christian https://orcid.org/0000-0003-1746-3020

References

Antolin, P., De Moortel, I., Van Doorsselaere, T., & Yokoyama, T. 2017, ApJ, 836, 219
Antolin, P., & Van Doorsselaere, T. 2019, FrP, 7, 85
Bate, W., Jess, D. B., Nakariakov, V. M., et al. 2022, ApJ, 930, 129
Beck, C., & Choudhary, D. P. 2020, ApJ, 891, 119
Bel, N., & Leroy, B. 1977, A&A, 55, 239
Bobra, M. G., Sun, X., Hoeksema, J. T., et al. 2014, SoPh, 289, 3549
Brisken, W. F., & Zirin, H. 1997, ApJ, 478, 814
Cauzzi, G., Reardon, K., Rutten, R. J., Tritschler, A., & Uitenbroek, H. 2009, A&A, 503, 577
Cavallini, F. 2006, SoPh, 236, 415
De Moortel, I., & Pascoe, D. J. 2012, ApJ, 746, 31
DeForest, C. E. 2004, SoPh, 219, 3
Edwin, P. M., & Roberts, B. 1983, SoPh, 88, 179
Gary, G. A. 2001, SoPh, 203, 71
Goossens, M., Erdélyi, R., & Ruderman, M. S. 2011, SSRv, 158, 289
Grant, S. D. T., Jess, D. B., Moreels, M. G., et al. 2015, ApJ, 806, 132
Grant, S. D. T., Jess, D. B., Zaqarashvili, T. V., et al. 2018, NatPh, 14, 480
Griem, H. R. 2005, Principles of Plasma Spectroscopy (Cambridge: Cambridge Univ. Press)
Hillier, A., Arregui, I., & Matsumoto, T. 2024, ApJ, 966, 68
Iroshnikov, P. S. 1964, SvA, 7, 566
Jafarzadeh, S., Rutten, R. J., Solanki, S. K., et al. 2017, ApJS, 229, 11
Jafarzadeh, S., Solanki, S. K., Gafeira, R., et al. 2017, ApJS, 229, 9
Jess, D. B., Jafarzadeh, S., Keys, P. H., et al. 2023, LRSP, 20, 1
Jess, D. B., Keys, P. H., Stangalini, M., & Jafarzadeh, S. 2021, RSPTA, 379, 20200169
Jess, D. B., Morton, R. J., Verth, G., et al. 2015, SSRv, 190, 103

Jess, D. B., Pascoe, D. J., Christian, D. J., et al. 2012, ApJL, 744, L5
Jess, D. B., Reznikova, V. E., Van Doorsselaere, T., Keys, P. H., & Mackay, D. H. 2013, ApJ, 779, 168
Kraichnan, R. H. 1965, PhFl, 8, 1385
Kuridze, D., Verth, G., Mathioudakis, M., et al. 2013, ApJ, 779, 82
Landi Degl'Innocenti, E. 1982, SoPh, 77, 285
Leenaarts, J., Carlsson, M., & Rouppe van der Voort, L. 2012, ApJ, 749, 136
Leenaarts, J., Carlsson, M., & Rouppe van der Voort, L. 2015, ApJ, 802, 136
Lissajous, J. 1857, AnCPh, 51, 147
Liu, Z.-X., He, J.-S., & Yan, L.-M. 2014, RAA, 14, 299
Livingston, W., Harvey, J. W., Malanushenko, O. V., & Webster, L. 2006, SoPh, 239, 41
Loukitcheva, M., Solanki, S. K., Carlsson, M., & White, S. M. 2015, A&A, 575, A15
Lozitsky, V. G., Baranovsky, E. A., Lozitska, N. I., & Tarashchuk, V. P. 2018, MNRAS, 477, 2796
Magyar, N., Duckenfield, T., Van Doorsselaere, T., & Nakariakov, V. M. 2022, A&A, 659, A73
Magyar, N., & Van Doorsselaere, T. 2016, A&A, 595, A81
Magyar, N., Van Doorsselaere, T., & Goossens, M. 2017, NatSR, 7, 14820
Magyar, N., Van Doorsselaere, T., & Goossens, M. 2019, ApJ, 882, 50
Maltby, P., Avrett, E. H., Carlsson, M., et al. 1986, ApJ, 306, 284
Mein, N. 1977, SoPh, 52, 283
Molnar, M. E., Reardon, K. P., Chai, Y., et al. 2019, ApJ, 881, 99
Mooroogen, K., Morton, R. J., & Henriques, V. 2017, A&A, 607, A46
Morton, R. J., Mooroogen, K., & Henriques, V. M. J. 2021a, RSPTA, 379, 20200183
Morton, R. J., Sharma, R., Tajfirouze, E., & Miriyala, H. 2023, RvMPP, 7, 17
Morton, R. J., Tiwari, A. K., Van Doorsselaere, T., & McLaughlin, J. A. 2021b, ApJ, 923, 225
Morton, R. J., Verth, G., Fedun, V., Shelyag, S., & Erdélyi, R. 2013, ApJ, 768, 17
Morton, R. J., Verth, G., Hillier, A., & Erdélyi, R. 2014, ApJ, 784, 29
Morton, R. J., Verth, G., Jess, D. B., et al. 2012, NatCo, 3, 1315
Pandit, S., Wedemeyer, S., Carlsson, M., & Szydlarski, M. 2023, A&A, 673, A137
Pant, V., Magyar, N., Van Doorsselaere, T., & Morton, R. J. 2019, ApJ, 881, 95
Pesnell, W. D., Thompson, B. J., & Chamberlin, P. C. 2012, SoPh, 275, 3
Pietarila, A., Aznar Cuadrado, R., Hirzberger, J., & Solanki, S. K. 2011, ApJ, 739, 92
Prasad, A., Ranganathan, M., Beck, C., Choudhary, D. P., & Hu, Q. 2022, A&A, 662, A25
Riley, K., Hobson, M., & Bence, S. 2006, Mathematical Methods for Physics and Engineering (3rd ed.; Cambridge: Cambridge Univ. Press)
Rimmele, T. R., & Marino, J. 2011, LRSP, 8, 2
Ruderman, M. S. 2017, SoPh, 292, 111
Ruderman, M. S., Goossens, M., & Andries, J. 2010, PhPl, 17, 082108
Ruderman, M. S., & Terradas, J. 2015, A&A, 580, A57
Russell, A. J. B., Simões, P. J. A., & Fletcher, L. 2015, A&A, 581, A8
Scherrer, P. H., Schou, J., Bush, R. I., et al. 2012, SoPh, 275, 207
Schou, J., Borrero, J. M., Norton, A. A., et al. 2012, SoPh, 275, 327
Sharma, R., Verth, G., & Erdélyi, R. 2018, ApJ, 853, 61
Shenstone, A., & Blair, H. 1929, London Edinburgh Philos. Mag. & J. Sci., 8, 765
Shetye, J., Verwichte, E., Stangalini, M., & Doyle, J. G. 2021, ApJ, 921, 30
Shi, M., Van Doorsselaere, T., Antolin, P., & Li, B. 2021, ApJ, 922, 60
Soler, R. 2017, ApJ, 850, 114
Soler, R., Andries, J., & Goossens, M. 2012, A&A, 537, A84
Soler, R., Goossens, M., Terradas, J., & Oliver, R. 2013, ApJ, 777, 158
Soler, R., Oliver, R., & Ballester, J. L. 2011, ApJ, 726, 102
Spruit, H. C. 1982, SoPh, 75, 3
Stangalini, M., Giannattasio, F., Erdélyi, R., et al. 2017, ApJ, 840, 19
Sun, X. 2013, arXiv:1309.2392
Tarr, L. A., Kobelski, A. R., Jaeggli, S. A., et al. 2023, FrASS, 9, 436
Terradas, J., Goossens, M., & Verth, G. 2010, A&A, 524, A23
Terradas, J., Magyar, N., & Van Doorsselaere, T. 2018, ApJ, 853, 35
The SunPy Community, Barnes, W. T., Bobra, M. G., et al. 2020, ApJ, 890, 68
Thompson, W. T. 2006, A&A, 449, 791
Tiwari, A. K., Morton, R. J., Régnier, S., & McLaughlin, J. A. 2019, ApJ, 876, 106
Torrence, C., & Compo, G. P. 1998, BAMS, 79, 61
Tsiropoula, G., Tziotziou, K., Kontogiannis, I., et al. 2012, SSRv, 169, 181
Van Doorsselaere, T., Andries, J., Poedts, S., & Goossens, M. 2004, ApJ, 606, 1223
Van Doorsselaere, T., Gijsen, S. E., Andries, J., & Verth, G. 2014, ApJ, 795, 18
Van Doorsselaere, T., Goossens, M., Magyar, N., Ruderman, M. S., & Ismayilli, R. 2021a, ApJ, 920, 162
Van Doorsselaere, T., Goossens, M., Magyar, N., Ruderman, M. S., & Ismayilli, R. 2021b, ApJ, 910, 58
Van Doorsselaere, T., Li, B., Goossens, M., Hnat, B., & Magyar, N. 2020, ApJ, 899, 100
Vaughan, B. A., & Nowak, M. A. 1997, ApJL, 474, L43
Verth, G., & Jess, D. B. 2016, GMS, 216, 431
Verth, G., Terradas, J., & Goossens, M. 2010, ApJL, 718, L102
Weberg, M. J., Morton, R. J., & McLaughlin, J. A. 2018, ApJ, 852, 57
Wedemeyer, S., Bastian, T., Brajša, R., et al. 2016, SSRv, 200, 1
Wheatland, M. S., Sturrock, P. A., & Roumeliotis, G. 2000, ApJ, 540, 1150
Wiegelmann, T. 2004, SoPh, 219, 87
Wiegelmann, T. 2008, JGRA, 113, A03S02
Wiegelmann, T., Inhester, B., & Sakurai, T. 2006, SoPh, 233, 215
Wiegelmann, T., Lagg, A., Solanki, S. K., Inhester, B., & Woch, J. 2005, A&A, 433, 701
Wiegelmann, T., & Sakurai, T. 2021, LRSP, 18, 1
Wiegelmann, T., Thalmann, J. K., Inhester, B., et al. 2012, SoPh, 281, 37
Withbroe, G. L., & Noyes, R. W. 1977, ARA&A, 15, 363
Wootten, A., & Thompson, A. R. 2009, Proc. IEEE, 97, 1463
Zaqarashvili, T. V., & Skhirtladze, N. 2008, ApJL, 683, L91
Zhong, S., Nakariakov, V. M., Kolotkov, D. Y., et al. 2023, NatCo, 14, 5298